Simulation of Low Cycle Fatigue Behaviour of Nickel-Based Alloy at Elevated Temperatures

Harish Ramesh Babu, Marco Böcker, Mario Raddatz, Sebastian Henkel, Horst Biermann, Uwe Gampe

***Abstract*—**Thermal power machines are subjected to cyclic loading conditions under elevated temperatures. At these extreme conditions, the durability of the components has a significant influence. The material mechanical behaviour has to be known in detail for a failsafe construction. For this study a nickel-based alloy is considered, the deformation and fatigue behaviour of the material is analysed under cyclic loading. A viscoplastic model is used for calculating the deformation behaviour as well as to simulate the rate-dependent and cyclic plasticity effects. Finally, the cyclic deformation results of the finite element simulations are compared with low cycle fatigue (LCF) experiments.

***Keywords*—**Complex low cycle fatigue, elevated temperatures, IN718, viscoplastic.

I. Introduction

COMPONENTS of turbomachinery such as turbines and compressors are exposed to higher temperature conditions and undergo cyclic loading due to frequent start-up and shut down operations [1], [2]. At these thermo-mechanical loading conditions, the lifetime of the components plays a significant role. To understand or describe the failure effects, the behaviour of the material should be analysed in a detailed way. By analysing the material behaviour, one could understand not only the material characteristics but also support the prediction of the evolution of damage and the lifetime of the turbine components efficiently.

In this paper, the material considered for investigation is the nickel-based alloy INCONEL718 (IN718). Two different batches of IN718 are considered in this paper because of different application purposes. Material A from a forged source which is used in the power industry e.g. gas turbines, whereas Material B from a cast and wrought source which is used in the aviation industry e.g. aero engines. Materials from both suppliers are tested at temperatures of 400 °C and 630 °C at different strain amplitudes. Both suppliers use different heat treatment processes for manufacturing the forged blocks. LCF tests are carried out for the batches, to describe the effects of cyclic loading under strain-controlled uniaxial loading conditions.

In addition to the experimental investigations, Finite Element Simulations are carried out in the presented work, to study the effects of material nonlinearity in detail. Usually, the material exhibits viscous effects if the testing temperature is above half of the homologous temperature [3]. At these high-temperature conditions, the material will exhibit temperature- and strain-rate dependent effects as well as stress relaxation effects. Therefore, these effects should be considered while choosing the deformation model. Consequently, a viscoplastic material model is chosen and coupled along with a combined kinematic hardening and isotropic hardening or softening model.

Besides uniaxial LCF tests, additional tests are required for determining the material constants of the deformation model. To describe the rate effects, several experiments should be conducted especially at different strain rates and dwell times. Instead of conducting different tests separately, all these tests are combined in a so-called Complex Low Cycle Fatigue (CLCF) test [4]. Therefore, the material constants for the deformation model are determined through those CLCF data. For validating the material constants, Finite Element (FE) simulations are performed subjected to uniaxial cyclic loading conditions. In this work, the inbuilt material model of the commercial FE tool ANSYS® is used.

Finally, the results of the simulations are compared with experimental LCF results, and the lifetime is calculated through the well-known Manson-Coffin-Basquin's model.

II. Experimental Setup and Results

The material from supplier A is delivered in the form of a disc forging as shown in Fig. 1. Both batches are solution annealed, followed by a two-step ageing heat treatment. The uniaxial specimens are manufactured from the disc and used for LCF and CLCF experiments. They are designed to have a thin test gauge area of 7 mm in diameter as illustrated in Fig. 2. In addition to that, the surface of the gauge area is ground and polished to 3 µm roughness.

In order to get the static material properties of both batches, hot tensile tests are performed at 400 °C and 630 °C at a strain rate of $\dot{\epsilon} = 10^{-3}$ [1/s]. The strain ratio for the LCF test is considered as R_ε = -1. The uniaxial LCF fatigue tests are carried out according to ASTM-E606 [5]. Few additional specimens are also manufactured to investigate the influence of the material orientation.

Harish Ramesh Babu is with the Technische Universität Dresden, Institute of Power Engineering, Helmholtzstraße 14, 01069 Dresden, Germany (e-mail: harish.ramesh_babu@tu-dresden.de).

Marco Böcker is with the Technische Universität Bergakademie Freiberg, Institute of Materials Engineering, Gustav-Zeuner-Straße 5, 09599 Freiberg, Germany (e-mail: marco.boecker@iwt.tu-freiberg.de).

Mario Raddatz and Uwe Gampe are with the Technische Universität Dresden, Institute of Power Engineering, Helmholtzstraße 14, 01069 Dresden, Germany.

Sebastian Henkel and Horst Biermann are with the Technische Universität Bergakademie Freiberg, Institute of Materials Engineering, Gustav-Zeuner-Straße 5, 09599 Freiberg, Germany.

Fig. 1 Large forged disc from Supplier A

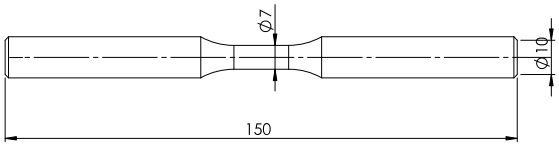

Fig. 2 Uniaxial LCF specimen

Uniaxial LCF and CLCF tests are conducted on servo-hydraulic test machine MTS Landmark 100. Inductive heating is used for heating the specimens. The temperature is measured with the help of two type K thermocouples which are attached within the gauge area. For measuring the strains, the two legs of a high-temperature extensometer are attached in the gauge sections as illustrated in Fig. 3. In the LCF test, a homogenous stress distribution occurs in the gauge section. Therefore, the mechanical stress σ can be calculated on the gauge sections.

Both batches are tested at different strain amplitudes, aiming at an average lifetime of the material for about 2000 and 20,000 cycles for both materials. The failure criteria in the tests are such that if the stress amplitude drops to about 10% relative to the formerly cyclically stabilized levels the corresponding cycles correspond to the crack initiation fatigue life.

A schematic plot of the CLCF test is shown in Fig. 4. The CLCF experiments are conducted at different strain amplitudes for both mentioned temperatures for both suppliers. The main idea of performing CLCF tests is that different test phases can be combined in a single test, saving testing time and thus also cost for manufacturing of specimens.

A typical CLCF test consists of two parts, aperiodic and periodic part. The aperiodic part is conducted with a constant strain amplitude (0.4%) at varying strain rates from $\dot{\epsilon} = 10^{-3}$ [1/s] to $\dot{\epsilon} = 10^{-5}$ [1/s]. At the end of each strain amplitude, a dwell time of thirty minutes is introduced on the tension and compression cycles, respectively. The same procedure is repeated at different higher strain amplitudes (0.6%, 0.8%) correspondingly. The periodic part begins after the completion of the aperiodic part. In the periodic part, the test is conducted at a constant strain rate ($\dot{\epsilon} = 10^{-3}$ [1/s]) with varying strain amplitudes until material failure occurs. The periodic part with its strain amplitude and its number of cycles will be used later for damage calculations.

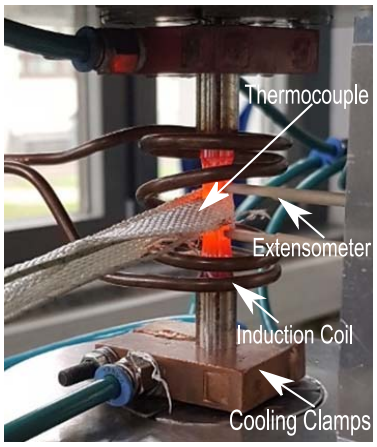

Fig. 3 Mounted specimen with extensometer, inductive heating coil, cooling clamps and two thermocouples, covered by a ceramic fabric

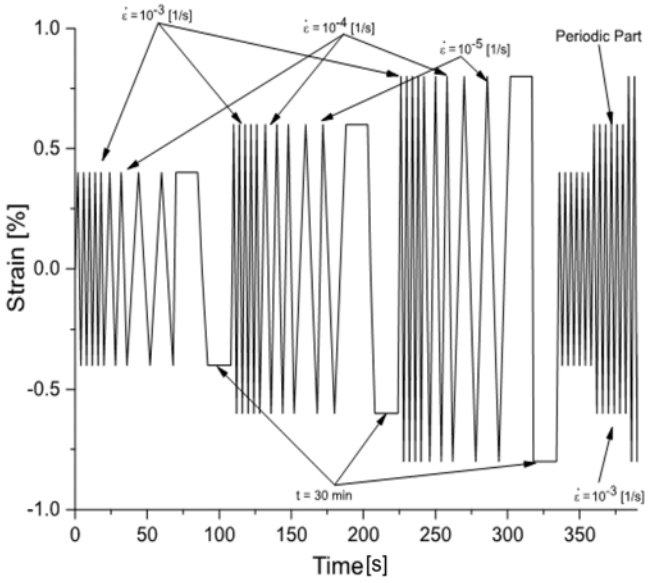

Fig. 4 Schematic plot of the CLCF test

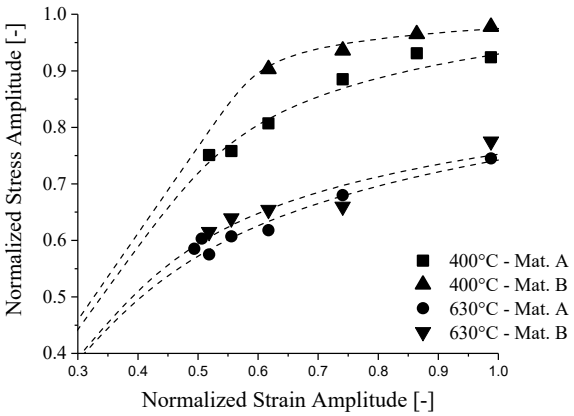

Fig. 5 Cyclic stress-strain curve of the LCF tests of a stabilized cycle at half lifetime with Ramberg-Osgood fit (lines)

The fatigue loading for the given strain amplitudes results in cyclic softening of the material over the number of cycles.

The stress amplitudes of stabilized cycles at the half lifetime, with cyclic softening and hardening in equilibrium, are shown in Fig. 5.

The cyclic stress-strain curve can be fitted using the Ramberg-Osgood Equation (1) as described in [6] and the normalized parameters from Table I.

$$\varepsilon_a = \frac{\sigma_a}{E} + \left(\frac{\sigma_a}{K'}\right)^{\frac{1}{n'}} \quad (1)$$

TABLE I
RAMBERG-OSGOOD FITTING NORMALIZED PARAMETERS

Temperature (°C)	Material	K'	n'
400	A	0.995	0.0758
400	B	1.002	0.0264
630	A	0.83	0.1334
630	B	0.825	0.1082

The lifetime of the LCF tests at both temperatures of 400 °C and 630 °C can be found in Fig. 6 for both materials A and B.

With the help of the Manson-Coffin-Basquin Equation (2), lifetime calculation was made for each material separately [7]. The constants in (2) are σ_f' - fatigue strength coefficient, b – fatigue strength exponent, ϵ_f' - fatigue ductility coefficient, and c – fatigue ductility exponent. The material constants were determined by regression of elastic and plastic parts of the experimental results.

$$\epsilon_{t,a} = \epsilon_{el,a} + \epsilon_{pl,a} = \frac{\sigma_f'}{E}(2N_f)^b + \epsilon_f'(2N_f)^c \quad (2)$$

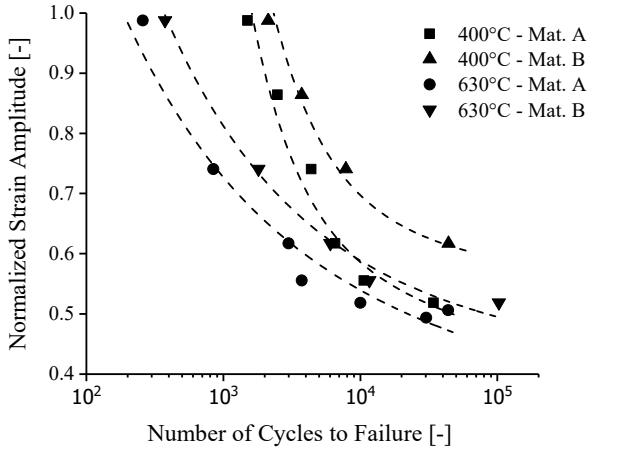

Fig. 6 Lifetime of the LCF tests with Manson-Coffin-Basquin fits (lines)

TABLE II
MANSON-COFFIN-BASQUIN NORMALIZED MATERIAL PARAMETERS FOR MATERIAL A AND MATERIAL B

Material Properties	MAT - A		MAT - B	
	400°C	630°C	400°C	630°C
σ_f'	179629.63	109259.259	150123.457	98641.975
b	-0.0606	-0.0410	-0.0250	-0.0232
ϵ_f'	6407.407	5.641	2530.864	9.9506
c	-1.20	-0.421	-1.05	-0.460

The Manson-Coffin Basquin fitting normalized parameters of the uniaxial LCF test for both materials are given in Table II.

III. DEFORMATION MODEL

After completing the experimental investigation, numerical simulations are conducted to describe the material behaviour of IN718 under uniaxial loading conditions at different strain amplitudes for both the suppliers. The simulations are performed using the commercial FE Analysis tool ANSYS® classic version (v18.2) with the inputs for the simulation programmed through an APDL script. The following deformation models are considered and combined to describe the effects of the material for both suppliers:

- Perzyna – Rate dependent model
- Chaboche – Kinematic hardening model
- Voce – Isotropic hardening/softening model

The material is assumed to be isotropic, and for small strains, the total strain ϵ is additively decomposed into an elastic part (ϵ_{el}) and plastic part (ϵ_{pl}) as described in (3). The elastic strain and stress satisfy Hooke's law (4), respectively.

$$\epsilon = \epsilon_{el} + \epsilon_{pl} \quad (3)$$

$$\sigma = \boldsymbol{E}:\epsilon_{el} \quad (4)$$

The model utilizes the von Mises yield criterion (5) to define the yield function along with the associated flow rule [3].

$$f = |\sigma - \alpha - \sigma_Y| \quad (5)$$

$$f = \left[\frac{3}{2}(S-\alpha):(S-\alpha)\right]^{\frac{1}{2}} - \sigma_Y \quad (6)$$

In (6), f defines the yield function which exceeds to zero in the case of rate-dependent plasticity where S denotes the deviatoric stress component, α – the back stress components, σ_Y – the isotropic hardening variable.

$$\dot{\varepsilon}_{pl} = \gamma\left(\frac{\sigma_{eff}}{\sigma_0} - 1\right)^{\frac{1}{n}} \quad (7)$$

The strain rate and stress relaxation effects are described through the rate-dependent Perzyna model as described in (7), where $\dot{\varepsilon}_{pl}$ – defines the plastic strain rate, γ – the viscosity parameter, σ_{eff} – the effective stress, σ_0 – the initial elastic limit, and n – the strain hardening exponent. The model will become rate-independent if γ tends to infinity, or the strain hardening exponent n approaches zero, or the plastic strain rate $\dot{\varepsilon}_{pl}$ approaches zero. For better convergence, the value of n stays between 0 and 1 as explained in [3].

$$\alpha = \sum_{i=1}^{n} \alpha_i \quad (8)$$

$$\dot{\alpha_i} = \frac{2}{3} C_i \dot{\varepsilon}_{pl} - \gamma_i \dot{\varepsilon}_{pl} \alpha_i \quad (9)$$

The cyclic hardening behaviour is described by the Chaboche kinematic hardening model as stated in (8) and (9), where α – refers to the back stress, while C and γ refer to kinematic hardening constants. In this work, three back stress models are taken into consideration to describe the hardening effect for the material. The user can utilize up to five models. However, for the current case, three models are found to be sufficient to describe the nonlinear hardening effects. The selection of the number of back stresses depends on the actual material behaviour and the strain range [8], [9]. For most of the ductile material, three models are sufficient.

To describe the cyclic hardening or softening effects of the material, the Voce isotropic equation should be used along with the kinematic hardening model described in (10):

$$\sigma_Y = \sigma_0 + R_0\dot{\varepsilon}_{pl} + R_\infty\left(1 - \exp\left(-b\dot{\varepsilon}_{pl}\right)\right) \qquad (10)$$

where R_0 – the linear part of the isotropic hardening is usually zero as stated in [3], [9]. R_∞ defines the cyclic hardening or softening behaviour. The parameter b governs the speed of saturation for the exponential term in the isotropic hardening equation. There is no damage model coupled with the deformation model.

A. Determination of Material Properties

Material parameters can be determined in different ways as described in [10]. However, in the current work, the material parameters are obtained through optimization with the experimental data. The initial values for the constants are determined according to [11] as well as [12], and the values are optimized on the basis of CLCF test results. Since the LCF test is conducted at isothermal conditions, all the material constants in the deformation model should be temperature-dependent. Hence, the material parameters are derived for each temperature for both batches. The FE tool, by default, has the capabilities of interpolating the values for the intermediate temperatures.

Elastic material properties: The E-Modulus is derived from the linear part of the stress-strain curve illustrated in [13]. The values for thermal conductivity and the coefficient of thermal expansion are adapted from the literature [14].

Hardening and softening material properties: As described previously, three back stresses (C_1, γ_1, C_2, γ_2, C_3, γ_3) are investigated. Thus, six material constants have to be determined. Initial values for C_1, C_2 and C_3 can be calculated from the stabilized cyclic stress-plastic strain curve. Likewise, the parameters $\gamma_1, \gamma_2, \gamma_3$ refers to the saturation of the curve; the higher the value of γ lower the saturation as stated in [15], [16].

The Chaboche kinematic hardening model is capable of simulating the ratcheting behaviour and is integrated into the back stress variables in a three-layer model, the γ – parameter in the third set controls the ratcheting behaviour. The ratcheting parameter can be determined from the uniaxial test with a different R ratio [17]. However, in the current scenario, all LCF tests are conducted with zero mean strain; resulting in low mean stresses. Thus, the ratcheting variable is optimized along with other kinematic hardening parameters. More about ratcheting effects is discussed in [18] and [19], respectively.

The initial elastic limit σ_0, can be predicted via the plastic part of the Ramberg-Osgood function. By keeping the plastic strain to a small value (e.g.1E-6) and by substituting the cyclic hardening and cyclic exponent (K' & n') values from Table I, the initial yield stress can be calculated as described in [13] and [20]. The R_∞ parameter can be found by calculating the difference between the peak stresses at the stabilized cycle to the peak stress at the first cycle [21]. If R_∞ tends to the positive value, then the hardening behaviour of the material can be described; if R_∞ is negative, then softening behaviour can be achieved. The parameter b defines the speed of saturation to the stabilized cycle. If b increases, then the saturation to the stabilization is reached faster, and vice versa [22].

Rate-dependent properties: The initial material constants γ, n are calculated through the procedure as described in [23], [24]. However, adapting these rate-dependent properties along with hardening properties is an iterative process, because the initial elastic limit is a common parameter in the deformation model, which may need to be varied several times accordingly.

B. Optimization Material Parameters

With the help of an in-house tool GAMO© the material constants are optimized [25]. The tool has two different algorithms, Levenberg-Marquardt and Monte Carlo sampling. The constitutive equation of the deformation model is fed into the optimization program in a one-dimensional form. Initial constants determined from the previous sections will be the start value for the optimization. The lower and upper bounds for the optimization are defined in such a way that the convergence can be achieved efficiently [26].

Before beginning the optimization, the experimental points should be reduced based on which type of material parameters have to be optimized [27]. For example, if the kinematic hardening parameters have to be optimized, more weightage should be provided to the cyclic stress-strain curve rather than the stress relaxation curve. Likewise, for rate-dependent properties, more weightage should be given for the stress relaxation experimental data. Finally, the experimental points are equally distributed for final optimization. Nevertheless, the isotropic softening parameters are not optimized through CLCF test. Instead, they have fitted to the max- and min stress points from the LCF experimental data. While optimizing the material parameters, care should be taken not only for the stress versus time profile but also for the stress versus strain profile.

The results of optimization for material B at 400 °C and 630 °C are shown in plots as normalized data points (Figs. 7 and 10). Similarly, the results of the stress-strain curves at different strain rates at 400 °C for both the materials are illustrated in Figs. 8 and 9. Apparently, at 0.4% of strain amplitude, there is hardly any sign of plastic opening for the material A at lower strain rates; thus, it is not described here. However, material B shows a very small opening of plastic

part at a strain rate of 10^{-4} per second.

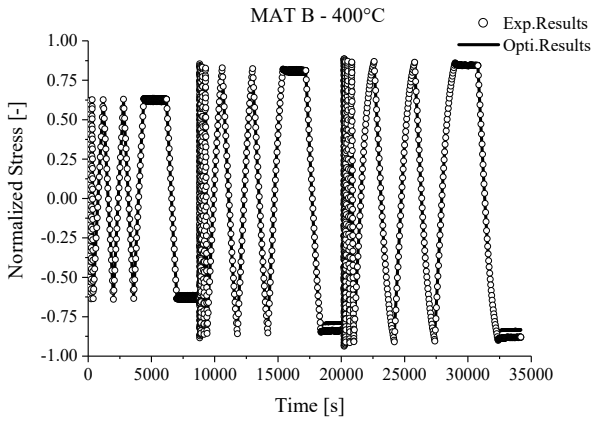

Fig. 7 Comparison of optimized and experimental stress versus time results for material B

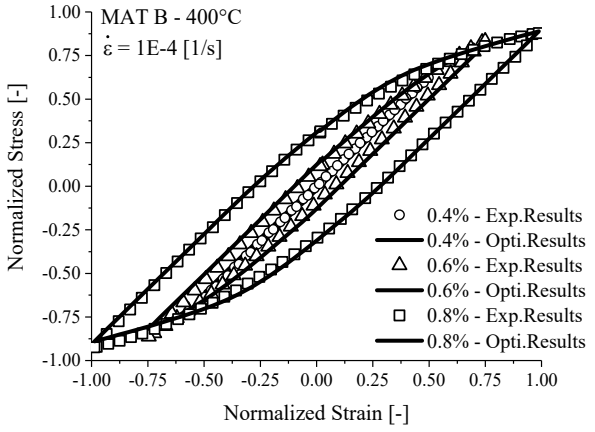

Fig. 8 Optimization results at a strain rate of 10^{-4} [1/s] compared with experimental results for material B

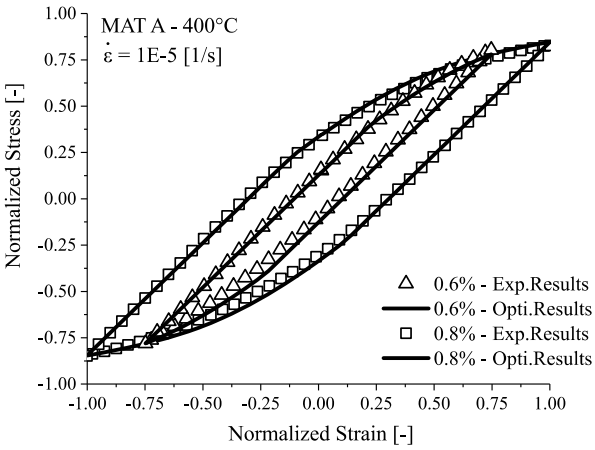

Fig. 9 Optimization results at a strain rate of 10^{-5} [1/s] compared with experimental results for material A

At the higher temperatures, especially at 630 °C (Fig. 10), both materials show more pronounced relaxation effects in the tensile and compression regime at higher strain amplitudes. This is due to the fact that there is a significant amount of accumulation of plastic strains at earlier cycles whereas at 400 °C, the material shows no relaxation effects even for higher strain amplitudes. Hence, the contribution of the viscous part is significantly lower when compared with higher temperatures.

Figs. 11 and 12 show the cyclic stress-strain curve at 630 °C for material A and B at different strain rates.

The width of the plastic region in the optimization is larger than the experiment points because of the parameter R_∞ in isotropic softening which is fitted through the LCF tests as explained before. Nevertheless, there is some slight deviation between the experiment and optimization in the compression part at lower strain rates, and this with increasing strain ranges. Finally, the mean deviation between the experiment and optimized results are calculated through (11) as stated in [28]:

$$\overline{X} = \frac{\sum_{i=1}^{m} | \sigma_{i,exp} - \sigma_{i,cal} |}{\sum_{i=1}^{m} | \sigma_{i,exp} |} * 100\% \quad (11)$$

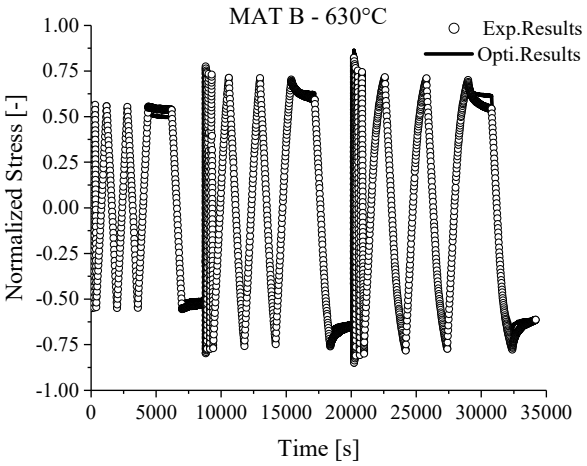

Fig. 10 Comparison of optimized and experimental stress versus time results at 630 °C for material B

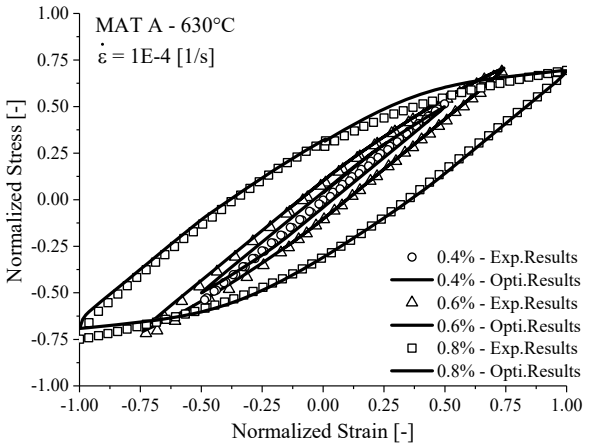

Fig. 11 Optimization results at strain rate for 10^{-4} [1/s] compared with experimental results for material A

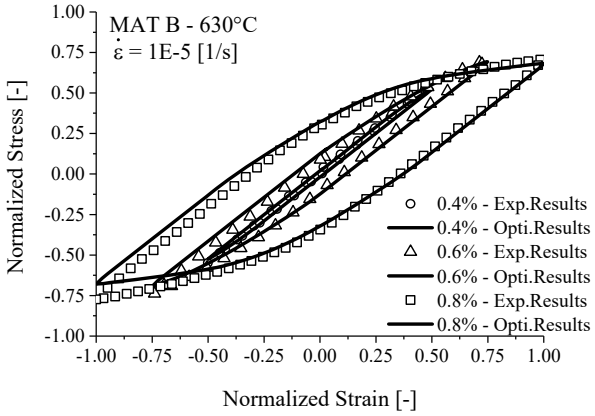

Fig. 12 Optimization results at a strain rate 10^{-5} [1/s] compared with experimental results for material B

TABLE III
OPTIMIZED MATERIAL CONSTANTS FOR SUPPLIER A

Material Properties	400 °C	630 °C
E(T)/E(515°) [MPa]	1.061	0.938
ν(T)/ν(515°) [-]	1	1
γ(T)/γ(515°)	1.981	0.018
n(T)/n(515°) [-]	0.119	1.880
σ_0(T)/ σ_0 (515°) [MPa]	1.423	0.576
C_1(T)/ C_1(515°) [MPa]	1.426	0.573
γ_1(T)/ γ_1(515°) [-]	1.407	0.592
C_2(T)/C_2(515°) [MPa]	0.124	1.875
γ_2 (T)/ γ_2(515°) [-]	0.860	1.139
C_3 (T)/C_3(515°) [MPa]	1.775	0.224
γ_3 (T)/ γ_3(515°) [-]	1.763	0.236
R_∞(T)/ R_∞(515°) [MPa]	1.160	0.839
b(T) / b(515°) [-]	0.775	1.224

TABLE IV
OPTIMIZED MATERIAL CONSTANTS FOR SUPPLIER B

Material Properties	400 °C	630 °C
E(T)/E(515°) [MPa]	1.076	0.923
ν(T)/ν(515°) [-]	1	1
γ(T)/γ(515°)	1.980	0.019
n(T)/n(515°) [-]	0.222	1.777
σ_0(T)/ σ_0 (515°)[MPa]	1.061	0.938
C_1(T)/ C_1(515°) [MPa]	1.915	0.084
γ_1(T)/ γ_1(515°) [-]	0.006	0.008
C_2(T)/C_2(515°) [MPa]	0.334	1.665
γ_2 (T)/ γ_2(515°) [-]	0.130	1.869
C_3 (T)/C_3(515°) [MPa]	0.140	1.859
γ_3 (T)/ γ_3(515°) [-]	0.366	1.633
R_∞(T)/ R_∞(515°) [MPa]	0.696	1.303
b(T) / b(515°) [-]	0.902	1.097

It is found that the mean deviation at 400 °C for material A and material B is 4.2%. Similarly, the mean deviation at 630 °C for material A is 6.7% and for material, B is 6.8%. The normalized material constants for material A and material B at both test temperatures are described in Tables III and IV. All the material constants are normalized with the corresponding material properties at temperature 515 °C.

IV. FE SIMULATION AND RESULTS

FE simulations are carried out after calculating all material parameters. As in the first step, the optimized material parameters are supplied to the FE tool. The gauge length of the LCF specimen is modelled as shown in Fig. 13. Only one-fourth of the LCF specimen gauge area is sketched due to symmetry. Solid185 element type is studied, and the geometry is discretized with the hexahedral eight-node element and three degrees of freedom [29]. For structural loading, symmetrical boundary conditions are applied (Y = 0 & Y = 90 under cylindrical coordinate system) to the structure. Similarly, at one end of the geometry (Z = 0) the displacement is fixed and on the other ends (Z = length of the cylinder) the cyclic displacement loading is applied. For thermal loading, the entire nodes of the geometry are applied with uniform temperature boundary conditions.

The analysis type is chosen to be quasi-static, and the load is incremented by finite steps such that convergence can be achieved. All the simulations are performed at a constant strain rate $\dot{\epsilon} = 10^{-3}$ [1/s] until stabilization. Since it is a uniaxial simulation, the entire geometry has a uniform stress distribution, due to which the stresses are on the axial direction of the geometry ($\sigma_{eqv} = \sigma_Z$).

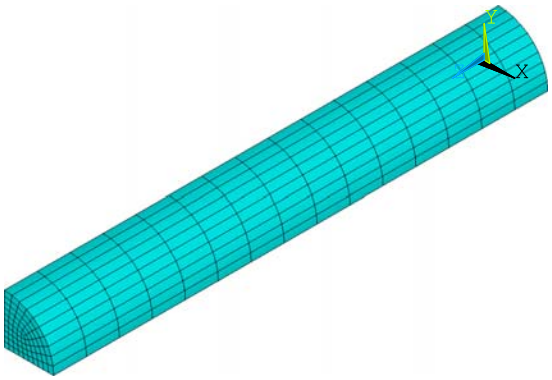

Fig. 13 Symmetric profile of LCF specimens used for FEM simulations

During cyclic loading, the equivalent stress is always positive; therefore there is a need for signed von Mises equivalent stress. This can be obtained by taking a scalar product between the sign of the first invariant (trace ($\boldsymbol{\sigma}$)) and von Mises equivalent stress amplitude. Thus, signed von Mises stress is used for illustration. The stabilized cycles are considered for post-processing, especially for lifetime calculation. This can be explained by the fact that once the simulation attains its stabilization, there will not be any hardening or softening effects on the stress-strain curve, thereby remaining the same. Since there is no damage model coupled with the deformation model, the curve remains stable.

The stabilized cycle results of FE simulations are compared with the LCF experiment results for Material A at 400 °C and 630 °C as described in Figs. 14 and 15.

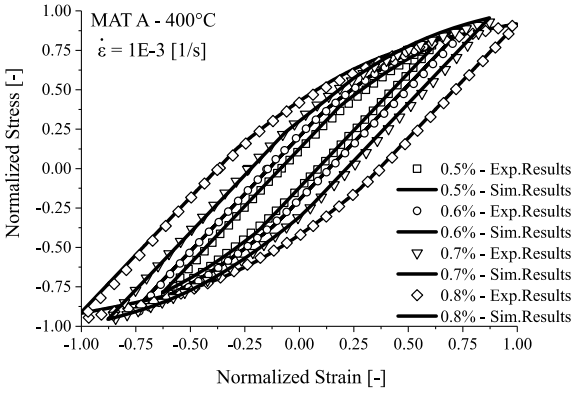

Fig. 14 Comparison of LCF experimental and FE simulations stabilized stress-strain hysteresis results for material A at 400 °C

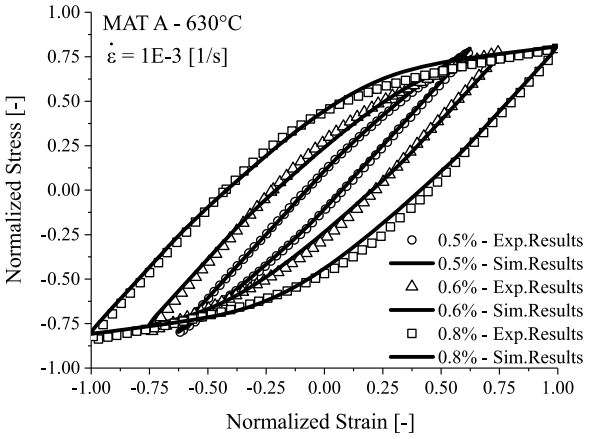

Fig. 15 Comparison of LCF experimental and FE simulations of stabilized stress-strain hysteresis results for material A at 630 °C

The results of material B are plotted in Figs. 16 and 17. For material B at 400 °C, at a strain amplitude of 0.5%, there is no significant softening effect visible while running the test, whereas the simulation slightly over predicts softening effects when compared with the experiment results. However, at higher amplitudes (0.6%, 0.7% and 0.8%), the stress-strain curves from the simulation show the exact behaviour of the experiment whereas for material A, the softening effects are visible at both lower and higher strain amplitudes.

The elastic and plastic strain values from the FE simulation are obtained from the stabilized cycles. With the help of material properties from Table II, along with the plastic part of the Manson-Coffin-Basquin Equation (2), the simulated lifetime values are calculated. The result of the FE simulation lifetime compared with the experimental lifetime ($N_f/2$) is illustrated in Fig. 18. The simulation of lifetime for both batches at test temperatures is within the scatter band of factor +-2.

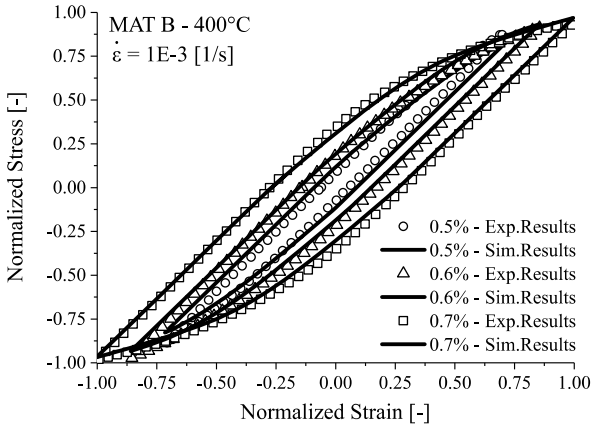

Fig. 16 Comparison of LCF experimental and FE simulations stabilized stress-strain hysteresis results for material B at 400 °C

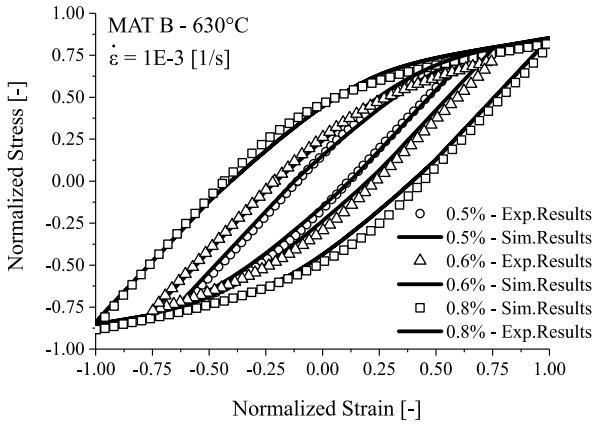

Fig. 17 Comparison of LCF experimental and FE simulations stabilized stress-strain hysteresis results for material B at 630 °C

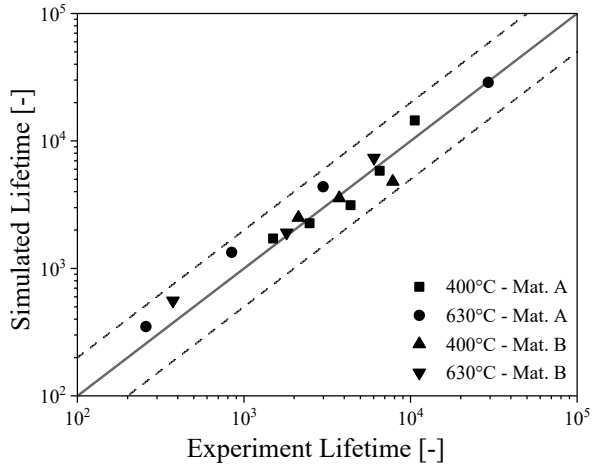

Fig. 18 Lifetime comparison of simulation and experiment for both materials at both test temperatures

V. Summary and Conclusion

In this paper, IN718 is investigated under uniaxial loading conditions at different test temperatures for two different material batches. A viscoplastic material model has been

considered to describe the cyclic deformation behaviour of the material. Furthermore, the process of selection of initial values and determining material parameters are presented. The results of optimization for both materials are discussed and found to be in good agreement with the experimental cyclic stress-strain behaviour. Likewise, the prediction of the isothermal LCF tests and FE simulations are coinciding well in terms of strength and life. Though the material model is capable of reasonably describing the temperature-dependent effects at both temperatures, further investigation may require coupling the static recovery and temperature rate effects in the kinematic- and isotropic-hardening equations. The predicted lifetime calculations are within the scatter band of two. As a next phase of the project, the obtained material parameters will be further validated for uniaxial TMF simulation.

ACKNOWLEDGEMENT

The research project "Lifing Methods, Multiaxial and Anisothermal" (LEBEMAN, No. 1288) is undertaken by the FVV (The Research Association for Combustion Engines eV). The research project is carried out in the framework of the industrial collective research programme (IGF no. 26EW). It is supported by the Federal Ministry for Economic Affairs and Energy (BMWi) through the AiF (German Federation of Industrial Research Associations eV) based on a decision taken by the German Bundestag. Besides, the authors would like to thank the companies Rolls-Royce Deutschland Ltd & Co KG, Siemens Gas and Power GmbH & Co. KG, and MTU Aero Engines AG for supplying material.

REFERENCES

[1] T. H. Guo, P. Chen, and L. Jaw, "Intelligent life-extending controls for aircraft engines," in *AIAA 1st Intelligent Systems Technical Conference*, 2004, vol. 2, no. September, pp. 910–919.

[2] J. E. A. Strake and C. A. de M. Branco, "Thermal mechanical fatigue of aircraft engine materials," in *Advisory Group for Aerospace Research & Development*, 1995, no. October, pp. 1–224.

[3] ANSYS Inc, "ANSYS Mechanical APDL Theory Reference," no. 724, p. 988, 2013.

[4] Andreas Jilg and T. Seifert, "HERCULES-2 Project TMF model for new cylinder head," pp. 1–17, 2018.

[5] ASTMInternational, "Standard Test Methods for Strain Controlled Fatigue Testing," *ASTM Standards, E606*, 2013. (Online). Available: ttp://www.astm.org/cgi-bin/resolver.cgi?E606E606M-19e1. (Accessed: 25-Oct-2020).

[6] W. Ramberg and W. R. Osgood, "Description of stress-strain curves by three parameters," 1943.

[7] O. H. Basquin, "The exponential law of endurance tests," 1910, vol. 10 TS-RI.

[8] R. Halama, J. Sedlk, and M. ofer, "Phenomenological Modelling of Cyclic Plasticity," *Numer. Model.*, 2012.

[9] J.-L. Chaboche, "Plasticity and Viscoplasticity under Cyclic Loadings," *Nonlinear Comput. Mech. - Course MP06*, no. March, pp. 1–60, 2009.

[10] T. Harth, "Identification of Material Parameters for Inelastic Constitutive Models: Design of Experiments," *Pamm*, vol. 3, no. 2, pp. 330–331, 2003.

[11] J. L. Chaboche, "Constitutive equations for cyclic plasticity and cyclic viscoplasticity," *Int. J. Plast.*, vol. 5, pp. 247–302, 1989.

[12] T. Bouchenot, C. Cole, A. P. Gordon, C. Holycross, and R. C. Penmetsa, "Application of noninteraction constitutive models for deformation of IN617 under combined extreme environments," *J. Eng. Mater. Technol. Trans. ASME*, vol. 140, no. 4, pp. 1–11, 2018.

[13] R. Hales, S. R. Holdsworth, M. P. O'Donnell, I. J. Perrin, and R. P. Skelton, "A code of practice for the determination of cyclic stress-strain data," *Mater. High Temp.*, vol. 19, no. 4, pp. 165–185, 2002.

[14] R. F. Muraca and J. S. Whittict, "Materials Data Handbook: Inconel Alloy 718," vol. 41. Western Applied Research & Development, Inc., pp. 165–194, 1972.

[15] J. Lemaitre, *Handbook of Materials Behavior Models*. Cambridge University Press, 2001.

[16] D. Nouailhas, "Unified modelling of cyclic viscoplasticity: Application to austenitic stainless steels," *Int. J. Plast.*, vol. 5, no. 5, pp. 501–520, 1989.

[17] P. Andrade, "Thermo-Mechanical Fatigue," *Ansys, Inc*, 2015.

[18] S. Bari and T. Hassan, "An advancement in cyclic plasticity modelling for multiaxial ratcheting simulation," *Int. J. Plast.*, vol. 18, no. 7, pp. 873–894, 2002.

[19] T. Hassan and S. Kyriakides, "Ratcheting in cyclic plasticity, part I: Uniaxial behaviour," *Int. J. Plast.*, vol. 8, no. 1, pp. 91–116, 1992.

[20] T. Bouchenot, B. Felemban, C. Mejia, and A. P. Gordon, "Application of Ramberg-Osgood plasticity to determine cyclic hardening parameters," *Am. Soc. Mech. Eng. Power Div. POWER*, vol. 2016-Janua, pp. 1–11, 2016.

[21] J. L. Chaboche, "A review of some plasticity and viscoplasticity constitutive theories," *Int. J. Plast.*, vol. 24, no. 10, pp. 1642–1693, 2008.

[22] N. O'Nora, T. Bouchenot, G. Geiger, and A. P. Gordon, "Constitutive modeling of TMF and creep-fatigue of a Ni-base alloy," *Proc. ASME Turbo Expo*, vol. 7A-2019, pp. 1–8, 2019.

[23] M. Thiele, U. Gampe, and K. Buchmann, "Accelerated material data generation for viscoplastic material models based on complex LCF and incremental creep tests," *Mater. High Temp.*, vol. 34, no. 5–6, pp. 311–322, 2017.

[24] M. Al-Haik, M. R. Vaghar, H. Garmestani, and M. Shahawy, "Viscoplastic analysis of structural polymer composites using stress relaxation and creep data," *Compos. Part B Eng.*, vol. 32, no. 2, pp. 165–170, 2001.

[25] M. Thiele, "Generic Damage and Material Model Optimization Program." TU Dresden - IET, Dresden, 2019.

[26] Y. P. Gong, C. J. Hyde, W. Sun, and T. H. Hyde, "Determination of material properties in the Chaboche unified viscoplasticity model," *Proc. Inst. Mech. Eng. Part L J. Mater. Des. Appl.*, vol. 224, no. 1, pp. 19–29, 2010.

[27] F. P. E. Dunne, J. Makin, and D. R. Hayhurst, "Automated procedures for the determination of high temperature viscoplastic damage constitutive equations," *Proc. R. Soc. A Math. Phys. Eng. Sci.*, vol. 437, no. 1901, pp. 527–544, 1992.

[28] T. Seifert, "Ein komplexes LCF-Versuchsprogramm zur schnellen und günstigen Werkstoffparameteridentifizierung," in *Tagungs Werkstoffprüfung*, 2006, pp. 409–414.

[29] Ansys Inc., "Element Reference Manual," vol. 15317, no. November. p. 1698, 2009.